Ultra-fast single-crystal CVD diamonds in the Particle Time-Of-Flight (PTOF) detector for low yield burn-history measurements on the NIF

B. Reichelt,[1, a)] R. Kishimori,[1] Y. Lawrence,[1] C. Wink,[1] M. Gatu Johnson,[1] T. Johnson,[1] P. Adrian,[2] K. Baker,[3] D. Casey,[3] D. Clark,[3] S. Dannhoff,[1] M. Eckart,[3] T. Evans,[1] H. Geppert-Kleinrath,[2] D. Gibson,[3] K. Hahn,[3] D. Higginson,[3] N. Izumi,[3] N. Kabadi,[4] S. Kerr,[3] J. Kunimune,[1] O. Landen,[3] E. Mariscal,[3] R. Marsh,[3] D. Martinez,[3] K. Meaney,[2] J. Pearcy,[1] R. Petrasso,[1] M. Rubery,[3] D. Rusby,[3] L. Russell,[1] D. Schlossberg,[3] V. Smalyuk,[3] R. Tommasini,[3] J. Frenje,[1] and C. Li[1]

[1)] *Massachusetts Institute of Technology, Cambridge MA 02139*

[2)] *Los Alamos National Laboratory, Los Alamos NM 87544*

[3)] *Lawrence Livermore National Laboratory, Livermore CA 94550*

[4)] *Laboratory for Laser Energetics, Rochester NY 14623*

(Dated: 26 October 2024)

The Particle Time of Flight (PTOF) diagnostic is a Chemical Vapor Deposition (CVD) diamond-based detector and is the only diagnostic for measuring nuclear bang times of low yield ($< 10^{13}$) shots on the National Ignition Facility (NIF). Recently, a comprehensive study of detector impulse responses revealed certain detectors with very fast and consistent impulse response with a rise time of < 50 ps, enabling low yield burn history measurements. At the current standoff of 50 cm, this measurement is possible with fast 14 MeV neutrons from deuterium-tritium (DT) fusion plasmas. PTOF-inferred DT burn width numbers compare well with widths inferred from the Gamma Reaction History (GRH) diagnostic on mid-yield ($10^{13} - 10^{15}$) shots, where both systems are capable of making this measurement. These new capabilities could be extended to 2.5 MeV DD neutrons from D plasmas and to even lower yield by reducing the detector standoff distance to 10cm; a design for this is also presented.

I. INTRODUCTION

The Particle Time of Flight (PTOF) diagnostic is regularly employed for measurement of nuclear bang times (time of peak emission) on the National Ignition Facility[1] (NIF) and is the only diagnostic capable of doing so at low yields $< 10^{13}$. PTOF consists of a Chemical Vapor Deposition (CVD) grown diamond with a voltage bias applied across it. When ionizing radiation strikes the diamond, charge carriers are excited into the conduction/valence bands, either by the radiation itself or by secondary "knock-on" products as is the case in neutrons and photons[2]. These freed carriers can be moved by the bias, resulting in a current that can be measured by an oscilloscope. Because any energy deposition in the diamond can free charge carriers, CVD diamonds are quite versatile for radiation measurement and can detect xrays, 14.7 MeV protons from the deuterium-helium-3 fusion reaction (D^3Hep), 2.45 MeV neutrons from the deuterium-deuterium fusion reaction (DDn), and 14.1 MeV neutrons from the deuterium-tritium fusion reaction (DTn). Aside from this versatility, CVD diamonds offer several advantages over other detector technologies, including resistance to radiation damage, a high bandgap that prevents scattered UV laser light from creating a strong signal background, and similar electron and hole mobilities, which decreases impacts of space charge.

Unlike many other uses of semiconductor radiation detectors, spectroscopic information is not important for PTOF. Instead, fast response is of utmost importance. Inertial Confinement Fusion (ICF) experiments produce extremely high particle fluences over short times (on the order of 100 ps), so many particles impact the detector at once. Thus, charge trapping effects, rather than being deleterious, are instead desirable for shortening the impulse response function (IRF) and obtaining faster time resolution[3]. For impulse responses with a rise time on the order of the burn width (~ 200 ps), the time resolution becomes fine enough to enable measurements of the burn history (emission as a function of time).

II. IMPULSE RESPONSE CHARACTERIZATION METHODOLOGY

One of the biggest impediments to a measurement of burn histories with PTOF is the question of how consistent impulse response is with a CVD diamond detector. To this end, impulse responses of the diamonds were characterized over a wide variety of conditions using the MegaRay facility at Lawrence Livermore National Labs. MegaRay is a linear electron accelerator that can produce 5ps bunches of electrons at a repetition rate of 10 Hz, and is thus able to provide high statistics measurements of impulse response.

An illustration of the physical setup at MegaRay is shown in fig 1 (a). Measurements were done with a direct and indirect setup as shown in fig 1 (b) and (c). In the direct setup the electron beam directly impinges upon the detector assembly, whereas in the indirect setup a thin Ta foil is placed in the path of the beam with the detector off axis, resulting in a mix of bremsstrahlung

[a)] Electronic mail: blr@mit.edu.

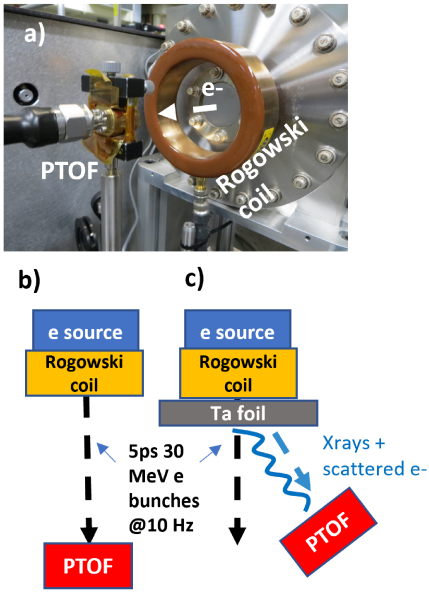

FIG. 1. Illustration of the experimental setup used to measure the impulse response of PTOF at the MegaRay electron accelerator: a) picture of the direct setup, with electron beam emerging from the beryllium window of MegaRay, b) Diagram of this direct setup, c) diagram of the indirect setup.

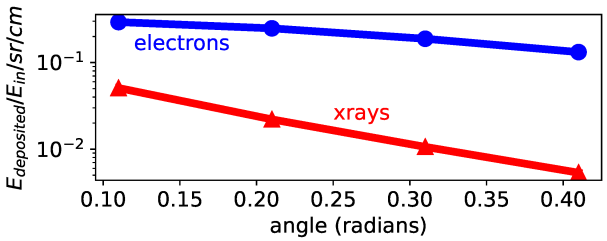

FIG. 2. Geant4 simulated energy deposited in detector per unit of energy in the electron beam, unit detector thickness, and detector solid angle relative to the electron beam spot on the Ta foil as the angle from electron beam axis to detector is varied. The deposited energy is given for electrons in blue and xrays in red assuming 30 MeV electrons incident on a 1500 μm thick Ta foil.

photons and scattered electrons impinging upon the detector. This setup allowed for smaller signals (below the detector saturation regime) to be probed while maintaining short signal impulses.

To obtain absolute detector sensitivities, Monte Carlo simulations of the indirect setup utilizing Geant4[4–6]. These simulations assume all electrons from the accelerator beam impinge upon the center of the tantalum foil, which is a good approximation as the beam spot was measured to be about 1 cm in diameter. Fig 2 indicate that the indirect setup deposits more energy in the detector through scattered electrons than xrays for a wide range of angles and foil thicknesses. These calculations are obtained by summing the energy deposited by each tallied particle at the detector location, where the deposited energy per unit detector thickness by an electron is $dE/dx_{collisional}(E_e)$ and for an xray is $E_\gamma \mu_{en}(E_\gamma)$. Here $E_{e/\gamma}$ is the energy of the particle at the detector, $dE/dx_{collisional}$ is the collisional stopping power for an electron[7], and $\mu_{en}(E_\gamma)$ is the mass energy absorption coefficient for photons[8]. For these highly relativistic electrons, energy is deposited volumetrically and so energy deposition can be normalized by the volume of the detector. Electron beam strength on some shots was measured with a Rogowski coil, allowing for an absolute sensitivity calibration when combined with the Geant4 energy deposition predictions.

In addition to the variation in signal strength, cable chain components, filtering, housing, bias, and diamond orientation were all varied in order to probe the response of PTOF detectors to different variations that may come up in experiments.

The diamonds used in the PTOF detectors are in the shape of disks and supplied by Applied Diamond and Diamond Materials GmbH and had circular, planar electrodes on the top and bottom consisting of 200 nm Ti, 200 nm Pt, and 1000 nm Au. This set of electrode materials in the past has been shown to provide an Ohmic contact that resists corrosion and inhibits diffusion between the different electrode layers[9]. Table I lists the dimensions of the detectors considered in this paper– the electrodes ranged from 6-9 mm in diameter and had thicknesses from 0.5-1.0 mm. The diamonds are optical grade with no intentional doping– the main impurity in the diamond is expected to be nitrogen at < 1 ppm, although the exact number was not measured by the manufacturer. The signal from the PTOF detector was carried along $<$ 8m of high bandwidth UFB293 cable to minimize signal distortion due to the cable chain– with this cable chain there should be < 5 dB attenuation up to 10 GHz. The PTOF detector is biased utilizing a Picosecond Pulse Labs Model 5531 HV Bias T, which has a bandwidth of 10 GHz. Both the Rogowski coil signal and PTOF signal were measured with a Keysight DSO-S 804A 8 GHz, 20 GSa/s oscilloscope.

Capacitance of the diamonds was measured using a BK Precision 875A LCR meter. The capacitance calculated for the diamond was calculated as the difference between the capacitance of the total detector and measurement assembly including the diamond minus the capacitance of the detector housing and measurement assembly without the diamond present. The results are summarized in Table I and it should be noted that the measured capacitance are higher than expected from the detector geometry alone due to capacitive coupling between the diamond and the housing. PCD/SCD 3 were not available to test the capacitance of, and thus were estimated from detectors of the same size.

An alternative in-situ measurement of impulse response utilizes timing shots at the NIF, where ultra short laser-pulses impinging upon high-Z targets produce $<$ 50 ps pulses of hard xrays. The combination of detector

TABLE I. Properties for detectors discussed in the text. From left to right, it shows the area covered by the electrode, the diamond thickness, the measured capacitance of the detector, the 20-80 rise times calculated from raw scope traces, the 80-20 fall times calculated from raw scope traces, and the carrier recombination time calculated for each detector– the last three of which are taken at a bias of -500V.

detector	electrode area [mm^2]	diamond thickness [mm]	detector capacitance [pF]	rise time [ps]	fall time [ps]	calculated τ_r [ps]
PCD 1	64	0.5	9.3 ± 0.14	86 ± 3	710 ± 20	105 ± 5
PCD 2	64	1.0	5.1 ± 0.14	53 ± 5	400 ± 6	98 ± 6
PCD 3	64	1.0	~ 5.1 (est.)	64 ± 3	500 ± 20	~ 150
SCD 1	28	1.0	2.6 ± 0.14	50 ± 8	200 ± 40	39 ± 7
SCD 2	28	1.0	2.7 ± 0.14	46 ± 9	190 ± 20	22 ± 15
SCD 3	28	1.0	~ 2.7 (est.)	47 ± 1	230 ± 10	~ 40

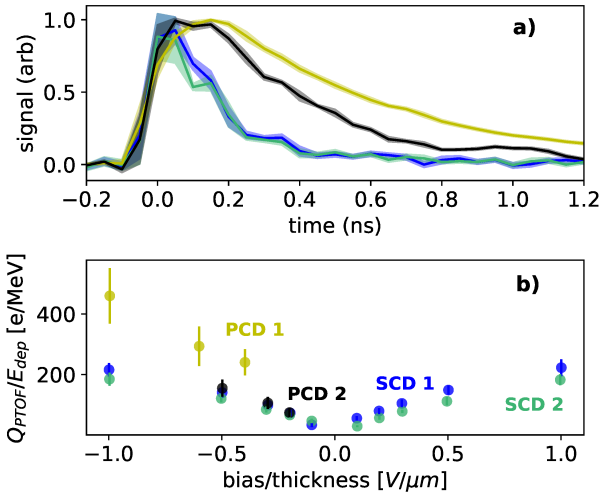

FIG. 3. a) Average of 1024 normalized IRFs at -500V bias for poly-crystalline detectors (PCDs) in yellow and black and single crystal detectors (SCDs) in blue and green. The error band thicknesses are given by the point-wise standard deviation of these waveforms. b) Charge liberated per MeV deposited energy for the same set of detectors

IRF measurements at MegaRay and in-situ PTOF IRF measurements at the NIF allows characterization of the NIF cable chain. Analysis from NIF shots where PTOF was run also allow for studying the impact of different particle types on detector response. Additionally, work is being conducted to enable single particle IRF measurements which would allow measurement with a more compact setup and less equipment[10].

III. IMPULSE RESPONSE CHARACTERIZATION RESULTS

A. Fast single crystal detectors

Testing at the MegaRay facility revealed a set of single-crystal diamonds with a very fast impulse response, as demonstrated by the blue and green IRFs in fig 3 a. These IRFs are each the point wise average of $\sim$ 1024 linearly interpolated waveforms normalized by peak amplitude and shifted to have the 50% rise at t=0. The error bands are similarly given by the pointwise standard deviation. Table I summarizes measured rise and fall times extracted from these waveforms at -500 V bias in the indirect setup. These detectors have a rise time (20-80% of peak voltage) of 50 ps and potentially much smaller since this is the sample rate of the oscilloscope used.

Detector sensitivity is displayed in fig 3 b demonstrating that more charge is generally captured for diamonds with a longer carrier lifetime. The sensitivity is defined as charge collected from the detector $Q = \int V(t)dt/50\ \Omega$ (where $V(t)$ is the voltage signal and 50 Ω is the scope impedance), divided by energy deposited in the detector which is calculated by multiplying the values from fig 2 by detector solid angle, thickness, and the input beam electron energy measured with the Rogowski coil. Only PCD/SCD 1-2 are depicted on this plot as other data was taken on a different day where the Rogowski coil was not available for absolute sensitivity calibration. Additionally, time constraints only allowed for measuring the PCD responses with negative bias, which was chosen as it is the same bias polarity used on the NIF.

Further investigation into the physics of PTOF detectors is necessary to make sense of the difference in behavior noted between different detector types. From the Shockley-Ramo theorem, charge collected due to mobile charge carriers in between the plates of a parallel capacitor is given by[11]:

$$Q = (E_{dep}/E_{eh})e\frac{d}{D} = (E_{dep}/E_{eh})e\frac{\mu E \tau_r}{D}, \qquad (1)$$

where Q is the total charge collected, E_{dep} is energy deposited collisionally in the diamond, E_{eh} is the energy required to free an electron hole pair (nominally 13 eV)[12], d is the distance charge carriers separate before recombining, and D is the diamond thickness. In eqn 1, d is expanded as $\mu E \tau_r$, where $\mu = \mu_n + \mu_p$ is the combined electron and hole mobility, E the electric field strength in the diamond, and τ_r the carrier lifetime before recombining. E is taken to be V_b/D throughout

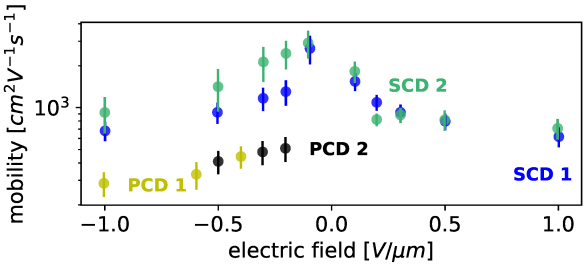

FIG. 4. Diamond mobility vs electric field for SCDs (blue and green) and PCDs (yellow and black)

the diamond, where V_b is detector bias voltage. This should be a good approximation– combining the 1D equations for current density in the diamond (ignoring diffusion current) $J = eE(\mu_p p + \mu_n n)$ and Poisson's equation $dE/dx = e(p-n)/\epsilon$ we obtain:

$$J = eE\left[\frac{\epsilon}{e}\frac{dE}{dx}(\mu_p - \mu_n) + (n\mu_p + p\mu_n)\right] \tag{2}$$

where n and p are electron and hole densities and ϵ is the permittivity of the diamond. Right before charge carriers are freed, $\epsilon/edE/dx \approx (p-n)_{eqm}$. This is a very small number due to the high bandgap of diamond– later it will be shown that it is $< 10^6 \mathrm{cm}^{-3}$ small enough that $E/(dE/dx) \gg D$ and E is essentially constant even before charge carriers are freed. Thus, J is dominated by the contribution from the second term, and since the electrons are highly relativistic and interact very evenly throughout the diamond, n and p are also constant, leading to a constant current and no space charge effects. Additionally, $\mu_n \approx \mu_e$ in diamond, further suppressing the dE/dx term[12].

To find τ_r, a circuit model is constructed that relates the measured waveform shape to τ_r. The detector is modeled as a capacitor of capacitance C in parallel with a resistor of time varying resistance $R = R_0 \exp(t/\tau_r)$ for $t > 0$ and a transmission line. Here, R_0 is the initial resistance of the diamond generated by the freed charge carriers. The current through the end of the transmission line is given by $i_L = (V - V_b)/Z_L$, where $Z_L = 50\ \Omega$ is the characteristic impedance of the transmission line and V is the voltage across the three components. The bias offset in i_L is due to the fact that the transmission line is modeled by the telegraphers equations, a pair of linear wave equations for the voltage and current which admits the steady state solution of $V_L(x) = V_b$ and $I_L(x) = 0$. The time varying solution of the line is then captured as the deviation from this equilibrium, which is also a solution due to linearity. Using Kirchhoff's current law, the equation governing the voltage is:

$$\frac{dV}{dt} = -V\left(\frac{\exp(-t/\tau_r)}{\tau_{RC}}\right) + \frac{V_b - V}{\tau_{ZC}}; V(0) = V_b, \tag{3}$$

where $\tau_{RC} = R_0 C$ and $\tau_{ZC} = Z_L C$ are time constants of relaxation.

Eqn 3 admits no general solution of elementary functions. However, the small signal limit does have an analytical solution. To see this, reformulate eqn 3 in terms of the variables $V \to \Delta V = 1 - V/V_b$ and $t' = t/\tau_{ZC}$, and for brevity denote the resulting $(\tau_{ZC}/\tau_{RC})\exp(-t/\tau_r)$ as $G(t')$ to get the non-dimensional equation

$$\Delta\dot{V} = (1 - \Delta V)G(t') - \Delta V; \Delta V(0) = 0. \tag{4}$$

If $\Delta V \ll 1$, $(1 - \Delta V) \to 1$ the resultant family of solutions can be found by integrating factors, which after substituting back for t is given by

$$\Delta V = \frac{\tau_r \tau_{ZC}}{\tau_{RC}(\tau_r - \tau_{ZC})}\left[\exp\left(-\frac{t}{\tau_r}\right) - \exp\left(-\frac{t}{\tau_{ZC}}\right)\right] \tag{5}$$

This family of solutions exhibits measurable differences even for τ_r significantly less than τ_{ZC}, especially relating to the width of the top of the curve. Thus, by fitting τ_r such that the χ^2 deviation from the measured signal is minimized, τ_r can be extracted with high precision– example values at -500 V bias are shown in table I. The error bars are given as the sum in quadrature between the standard deviation of the fit τ_r values for a collection of waveforms and half the change in the average τ_r observed when the measured capacitance moves from the lower to upper error bound.

Once τ_r is found, the average mobility of charge carriers in the diamond can be determined using eqn 1 and calculated Q_{PTOF}/E_{dep} values. Higher mobility is seen for the SCDs compared to PCDs, with low bias values of $\sim 2500\ \mathrm{cm}^2\mathrm{V}^{-1}\mathrm{s}^{-1}$ and $\sim 500\ \mathrm{cm}^2\mathrm{V}^{-1}\mathrm{s}^{-1}$ respectively. The SCD values are similar to those measured for natural diamonds in previous literature, while the lower mobility for PCDs has also been seen in the past[13]. This lower mobility comes despite the higher sensitivity of the PCDs – the reason for this is due to the much shorter carrier lifetime for the SCDs. This result suggests the mobility limitation is caused by scattering off of imperfections in the lattice and at grain boundaries, which is enhanced in the PCDs. However, the longer carrier lifetimes for the PCDs suggests that grain boundaries are not the dominant property controlling recombination.

Additionally, theory and dark current measurements suggest that both large numbers of deep traps in the diamond and a Fermi level close to the level of these traps are essential for fast detector response. Isolated nitrogen impurities in diamond result in a donor level 1.7 eV below the conduction band, providing a site for recombination through the Shockley-Read-Hall (SRH) mechanism[14–16]. Recombination via the SRH mechanism occurs when either an electron falls from the conduction band into a deep trap state (capturing an electron), or when an electron occupying a deep trap falls into the valence band (capturing a hole). The SRH mechanism is crucial for

recombination in an indirect bandgap material like diamond, as it allows conservation of momentum. The dynamics of charge carrier recombination in typical experiments are fundamentally non-equilibrium processes, so the quantities of merit are the net recombination rates for electrons and holes out of equilibrium[15]:

$$\begin{aligned}\frac{dn}{dt} &= -n\langle\sigma_{nt}v_n\rangle N_t(1-f_t) + A_n \\ \frac{dp}{dt} &= -p\langle\sigma_{pt}v_p\rangle N_t f_t + A_p \\ \frac{df_t}{dt} &= \left(\frac{dp}{dt} - \frac{dn}{dt}\right)/N_t,\end{aligned} \tag{6}$$

where $n(p)$ is the free electron (hole) concentration, $\langle\sigma_{nt(pt)}v_{n(p)}\rangle$ is the distribution averaged electron (hole) trapping probability, N_t is the trap concentration, f_t is the fraction of traps occupied by electrons, and $A_{n(p)}$ is the rate of spontaneous detrapping of electrons (holes). In equilibrium, the detrapping terms are balanced with the other two, so when additional carriers are injected due to stopping of a charged particle in the diamond, the trapping terms initially dominate the carrier evolution. It is clearly important that N_t be sufficiently large to facilitate recombination, as the recombination rates for both holes and electrons are both proportional to it.

The system of equations in 6 always lead to the most efficient recombination when $dn/dt = dp/dt$, since the third equation eventually drives them into equilibrium after some characteristic time[15]. This leads to an optimal Fermi level for maximizing recombination speed such that

$$f_t = \frac{n\langle\sigma_{nt}v_n\rangle}{p\langle\sigma_{pt}v_p\rangle + n\langle\sigma_{nt}v_n\rangle}. \tag{7}$$

The precise value of this constant varies, as the trapping probabilities of electrons and holes are different and different areas of the diamond will have more electrons than holes or vice versa as the charge carriers are swept out by the bias. The literature[13] suggests $\langle\sigma_{nt}v_n\rangle \approx 1000\langle\sigma_{pt}v_p\rangle$. This information, along with the fact that the total number of holes created is about the same as the number of electrons, means that recombination is optimally fast with large N_t and a Fermi level such that $f_t \approx 0.999$. This can be achieved by a Fermi level ~ 0.17 eV above the nitrogen trap level. Although these diamonds were not intentionally made to satisfy this condition, such a state could be reliably manufactured by using a p-type dopant like boron at 0.1% the nitrogen dopant level, which can be seen graphically by plotting carrier densities as a function of Fermi energy and noting the true Fermi energy will be the one that enforces neutrality[17].

Aside from high nitrogen doping and light acceptor doping, it is also important that the crystal be free of defects like dislocations and stacking faults that can cause

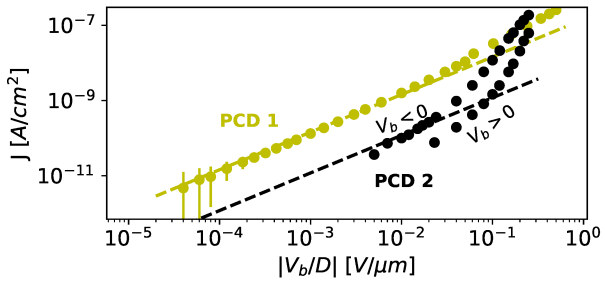

FIG. 5. Dark current curves for PCDs, plotted as current density vs linear electric field estimate (bias voltage divided by detector thickness). PCD 2 has both positive (lower) and negative (upper) bias curves plotted, while PCD 1 has only the negative bias curve as the positive and negative bias curves are too similar to distinguish. Dotted lines are ohmic fits using mobility values from fig 4 at -200V bias for carrier densities of 1.8×10^5 cm^{-3} and 1.5×10^4 cm^{-3}, respectively. The SCDs saw no measurable current at any bias.

shallow donor states in the diamond, as even a small number of shallow traps pull the Fermi level up much higher and lead to $f_t \approx 1$ and poor electron recombination properties. An illustration of this point is given in fig 5, which shows dark current JV curves measured via a Keithley 6517b electrometer for PCD 1 and PCD 2. PCD 1 had a response that was essentially the same in positive and negative bias, while PCD 2 had a JV curve shifted down by $\sim 5\times$, indicating an anisotropy in diamond properties, likely related to the growth of grain size from the nucleation to growth side.

These curves are expected to have three regions: an ohmic region at low voltages where equilibrium carriers dominate that has a V dependence, a trap-filling region at moderate voltages varying as V^{l+1} where $l > 1$ as charge is injected into the device and raises the Fermi level via the filling of traps, and a space charge limited current region once all traps are filled[18]. However, as noted earlier, the low concentration of carriers means that J the space charged limited region is still expected to be proportional to V.

It can be seen in the figure that a measurable equilibrium carrier concentration is present for the slower polycrystalline diamonds since there is a measurable ohmic current. As discussed earlier, dE/dx is expected to be very small given the low equilibrium carrier density, and the dE/dx term can be discarded from eqn 2 to find $I_{Ohm} = Aen_{eqm}\mu V/D$ and mobility values at the smallest biases from fig 4 of $\sim$ 500 cm^{2}V^{-1}s^{-1}, the PCDs are shown to have equilibrium carrier densities of 1.8×10^5 cm^{-3} and 1.5×10^4 cm^{-3} in reverse bias, consistent with the assumption of small carrier densities. The beginnings of the trap filling regime is also present for the PCDs, both of which indicate that the Fermi level at equilibrium resides closer to the conduction band than the nitrogen trap level due to the presence of shallower

traps. Meanwhile, no currents at all can be seen for the fast single crystal diamonds, indicating $n_{eqm} < 50$ cm^{-3} and a Fermi level at equilibrium far away from the conduction band with a large number of trap states that must be filled before current is observed, consistent with the conditions for optimal trapping predicted by eqn 6.

B. Effects of large signal amplitude

An important requirement of eqn 4 is that it preserve convolutions of the conductance term $G(t')$, which characterizes the time dependent conductivity of the diamond in response to an impulse of radiation. Preserving convolutions on this term is then the property that if V denotes the solution of this equation when $G(t') = f(t')$, then $f * \Delta V_G = \Delta V_{f*G}$, where $*$ denotes convolution.

This is an important property because it is assumed in analysis of PTOF data that the response of the detector to a radiation signal $f(t')$ of non-zero duration is the convolution of the response to an impulse of radiation and the radiation signal. It can be shown that this is preserved when $\Delta V << 1$, in which case the equation approximately becomes $\Delta \dot{V} = G - \Delta V$. In this limit, preservation of convolutions can be shown most easily by taking the Fourier transform of $\mathcal{F}(\Delta V) = \Delta \hat{V}$ so that $\Delta \dot{V} \rightarrow i\omega \Delta \hat{V}$. This implies

$$\hat{f}\Delta\hat{V}_G = \hat{f}\frac{\hat{G}}{1+i\omega} = \Delta\hat{V}_{\hat{f}\hat{G}}, \tag{8}$$

as expected. However, if ΔV does not remain small, this property no longer holds and the usual analysis technique is invalid. Testing using the direct electron setup at MegaRay with SCD 3 revealed no measurable change in IRF shape up to $\Delta V = 0.2$, allowing for PTOF measurements up to $\sim 10^{15}$ DT-n. PCD 3 in the same setup showed more variability in the rise time, potentially due to the higher τ_r/τ_{ZC} ratio or changes in the charge transport within the diamond. In the future, the circuit model may provide parametrization for fitting to curves in the nonlinear regime.

C. NIF cable chain response

In-situ at the NIF, the PTOF IRF is not the raw response measured at MegaRay due to additional broadening from the cable chain. The NIF cable chain consists of 3.1 m of RG402, 11.4 m of UFB293C, 35 m of LMR-600, and 4.9 m of LL290HF, which combine to provide a significant broadening to the IRF. However, despite this cable chain broadening, xray timing shots at the NIF have confirmed that the fast detectors tested at MegaRay have significantly faster rise and fall times than the older detectors in use.

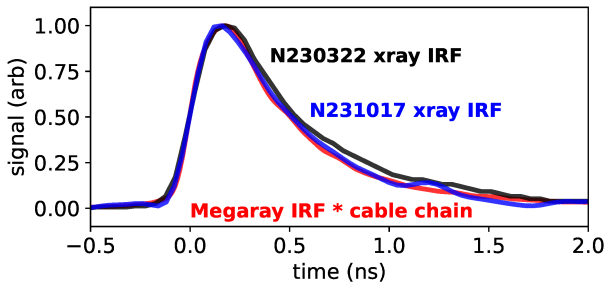

FIG. 6. Illustration of the stability of a fast single crystal detector in situ at NIF as well as accuracy of a cable chain model. The blue and black traces are two in situ (detector+cable) IRFs obtained at the NIF several months apart with the same detector, and the red trace is the Megaray IRF with the same filtering convolved with a cable chain IRF model.

The fact that one of the fast detectors has been fielded both at MegaRay and in-situ at the NIF allows for models of the NIF cable chain impulse response to be tested. Fig 6 demonstrates the impulse response of the fast single crystal detector measured on two different NIF timing shots, as compared to a MegaRay data convolved with the expected cable chain response calculated from a model. The measured data suggests that the impulse response is very stable over time for these detectors, changing by only 12 ps on the rising edge and 50 ps on the falling edge despite significant changes in the recording setup and several uses on DTn shots in the intervening time.

The cable chain model is constructed by treating each section of coaxial cable as a transmission line and calculating the transfer function based off of the geometrical and material information from the manufacturer[19]. The value for the dielectric loss of the material came from measurements in the literature of PTFE and polyethylene foam[20,21]. Even with the nominal manufacturer values, this model does a very good job at reproducing the NIF data, showing that it is feasible to measure IRFs at external facilities like MegaRay. They can then be convolved with the cable chain response constructed through models like these to obtain the full detector+cable chain IRF for use in analysis routines.

D. Filtering effects

It is usually the case on the NIF that PTOF is run with shielding, including Au, Ta, Al, and W ranging in thickness from 50 um to 3 cm. Generally the purpose of the shielding is to reduce background or to limit the size of a signal so that the detector stays within the linear regime. In particular, shots utilizing the high intensity Advanced Radiographic Capability (ARC) laser tend to produce very large xray signals that must be attenuated

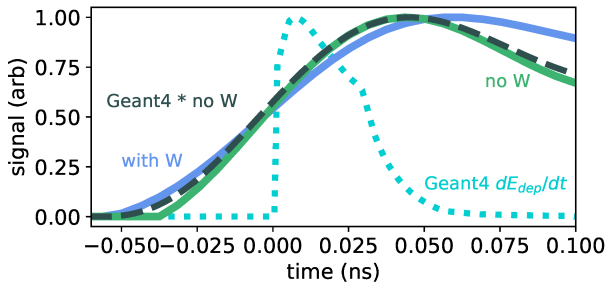

FIG. 7. Plot showing the impact of a 3 cm W filter on impulse response. Blue and green curves show the MegaRay-measured IRF with and without the filter, respectively. Turquoise shows the total energy deposition vs time as predicted from a Geant4 simulation using the same model for deposition discussed for fig 2. Dark grey gives the no filter IRF convolved with the Geant4 energy deposition. All timing offsets of curves are arbitrary as there was no absolute timing calibration for the IRFs.

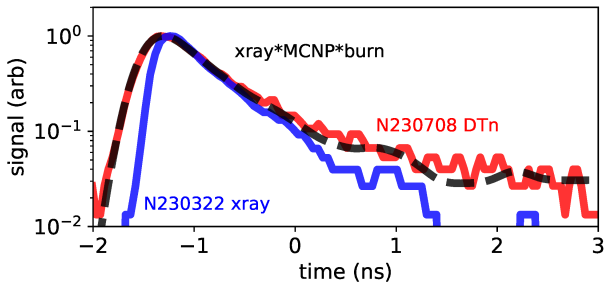

FIG. 8. Illustration of tail broadening on DT shots. The blue trace is PTOF data from an xray timing shot used to obtain an IRF, the red trace is a DTn shot, and the black trace is the timing shot IRF convolved with the neutron arrival history for neutrons in an MCNP calculation including the snout setup along with a Gaussian of FWHM 300 ps to account for burn history.

with thick W filtering, so understanding how this filtering affects impulse response is quite important to burn width measurements[22].

In order to probe this at MegaRay, a comparison was done between the IRF of PTOF in the indirect setup with no filtering and the IRF of PTOF in the direct setup with 3cm W filtering. The comparison was made between the direct and indirect setups to keep the signal in an appropriate range for both the filtered and unfiltered shots. The W filter introduces a clear broadening as shown in fig 7 as the difference between the "with W" and "no W" curves. Also shown in this plot for comparison is the Geant4 simulated total energy deposition vs time in the detector as predicted from a Geant4 simulation of 30 MeV electrons hitting a 3cm W cap using the same model for deposition in the diamond discussed for fig 2. When this energy deposition history is convolved with the no filter IRF, it is seen that the filter broadening predicted by Geant4 helps explain the early rising edge of the signal that is most important for burn width measurements, but cannot explain the late-time broadening of the IRF. It is possible this is due to missing physics in Geant4, such as the lifetime of longer lived excited states of the tungsten nucleus and inner electron shells.

In addition to the impact of xrays and charged particle filter interactions, neutrons scatter within thick W filtering, incurring time of flight broadening as their energy is decreased and travel path is lengthened. MCNP[23] simulations of this process with a 3 cm W filter reveal that it causes negligible broadening unlikely to interfere substantially with short burn width measurements of $\lesssim 5$ ps for DTn, and ≈ 50 ps for DDn. There is a long tail of late arriving neutrons that could cause distortion when deconvolution is performed on shots with long burn histories $\gtrsim 500$ ps. However, the late arriving neutrons from scattering in the filter are mostly low energy neutrons from large angle scatters that can't deposit much energy in the PTOF diamond.

E. Scattering off of snout

Like interactions with filtering, scattering off of other components in the snout assembly that PTOF is attached to can create a long lived tail of late arriving neutrons. Unlike scattering in the filter, the geometry of the snout allows these late arriving neutrons to have a low scattering angle and thus higher energies more likely to be detected by PTOF. These scattered neutrons are unlikely to interfere with the primary signal of unscattered neutrons in short burn width shots, but for campaigns with a long burn width it could pose a problem when deconvolution is performed. This effect is reflected in DTn burn history data, as illustrated in fig 8, which shows that the tail in DTn shots at the NIF has a longer decay time than the measured tail of xray timing shots. MCNP calculations performed for a representative snout assembly provide an arrival history for the DT neutrons that is convolved with the xray timing shot IRF and demonstrates that the tail of the resulting scatter-corrected IRF matches much more closely with the tail from a DTn shot. The difference in the rising edge comes from convolution with a Gaussian of FWHM 300 ps to account for the impact of time of flight broadening and emission history.

IV. METHODOLOGY OF BURN WIDTH RESPONSE

Most PTOF analysis is done with a forward fit procedure, in which the χ^2 error from a model signal given some burn history shape is minimized using gradient descent[24]. Mathematically, this is the minimization of:

TABLE II. Error budget for PTOF burn width measurement of DTn on NIF shots situated at 50 cm from TCC. The first column lists the source of the error, the second column is the amount by which the IRF is broadened by this error source, the third column is the width of the broadening component on its own, and the final column is the error in burn history width incurred by the error source assuming a fast single crystal detector. Bold values indicate which column has an intrinsic value in the sense that it remains the same for a detector with a different IRF width.

Origin of error	$\frac{\Delta W_{IRF}^2}{W_{IRF}}$ [ps]	$\sqrt{\Delta W_{IRF}^2}$ [ps]	ΔW_{burn} [ps]
IRF variability	**12**	55	–
n scatter in filter	0.1	**5**	–
γ response of filter	10	**50**	–
T_i uncertainty	**3**	27	–
distance uncertainty	**1**	16	–
total @ $W_{burn} = 100$ ps	–	–	32
total @ $W_{burn} = 200$ ps	–	–	16
total @ $W_{burn} = 300$ ps	–	–	11

$$\chi^2(\mu, W_{burn}, A) = \sum_i \frac{((B(\mu, W_{burn}, A) * I * T)_i - V_i)^2}{2\sigma^2} \tag{9}$$

Where the $*$ denotes discrete convolution, i is the time index, V_i is the measured signal at index i, and σ is the estimated noise of the scope signal. $B(\mu, W_{burn}, A)$ is a Gaussian burn history parameterized by mean time μ, the full-width half-max (FWHM) burn width W_{burn}, and amplitude A. I denotes the detector + cable IRF, while T is the time of flight (TOF) broadening of an impulse of neutrons due to the finite temperature of the fusion plasma. The TOF broadening can be calculated with ion temperature measurements from the Neutron Time of Flight (NTOF) diagnostic[25], and are typically $< 10\%$, leading to a $< 2.5\%$ uncertainty in the IRF width.

After finding the minimum, statistical error can then be estimated by assuming the three fit parameters and signal errors are Gaussian and taking the inverse Hessian of the chi-squared error at the minimum to be the covariance matrix of the fit parameters[24].

μ is known as the bang time and is often the only parameter measured by PTOF since the fit is typically highly insensitive to changes in W_{burn}, which is reflected as large statistical error bars. However, when using one of the fast diamonds mentioned in III A, the statistical fit error is typically quite small and the contribution to uncertainty on W_{burn} is dominated by uncertainty in the shape of the rising edge of the total IRF $I * T$.

To quantify this uncertainty, note that when fitting short burn widths, the burn history fit is dominated by the rising edge of the signal since that is the highest frequency component of the IRF. The IRF can be well modeled as a Gaussian convolved with a falling exponential set to zero for $t < 0$, and the commutativity and associativity of convolution mean that for error analysis, the exponential term can be ignored and fitting to a Gaussian burn history is essentially the convolution of two Gaussians.

In estimating the total error, the fact is used that $W_{burn} \approx \sqrt{W_{meas}^2 - W_{IRF}^2}$, W_{meas} is the FWHM of the Gaussian component of the measured signal, and W_{IRF} is the FWHM of the Gaussian component of the total system IRF including cable chain and time of flight broadening. The parameters for the Gaussian responsible for the rising edge of the IRF can be estimated by measuring rise time and using the conversion that FWHM $= 2.091\Delta t_{20\to80}$, leading to $W_{IRF} \approx 250$ ps. If Gaussian broadenings are applied to the IRF, $W_{IRF}^2 \to W_{IRF}^2 \pm \Sigma\Delta W_{IRF}^2$ where $\Sigma\Delta W_{IRF}^2$ is the squared sum of these broadenings. Thus, in the presence of broadenings W_{burn} becomes

$$\sqrt{W_{burn}^2 \pm \Sigma\Delta W_{IRF}^2} \approx W_{burn} \pm \frac{\Sigma\Delta W_{IRF}^2}{2W_{burn}} \tag{10}$$

In reality, the exact level of broadening can difficult to calculate, so if these broadenings is only approximately known, the uncertainty of the burn width is given by:

$$\Delta W_{burn} \approx \frac{\Sigma\Delta W_{IRF}^2}{2W_{burn}} \tag{11}$$

Using this analysis, an error budget has been constructed in table II guided by values taken from other sections of this paper. The IRF variability row comes from observed differences in the rising edge of fig 6 that are not explained by other sections of this paper.

V. EXPERIMENTAL RESULTS AT THE NIF

Measurements of DTn histories at the NIF were taken using one of the fast single crystal detectors with 3 cm of tungsten shielding. Analysis of the burn history was made using the forward fit procedure described above on shots with a variety of different burn widths. Changes to the rising edge of the IRF from filtering were not made and instead were accounted for as sources of uncertainty in table II. The tail of IRF used has been corrected for neutron scatter leading to better fits of the tails.

The result for a variety of different NIF shots is given in table III. A comparison is provided to the Gamma Ray History (GRH) diagnostic[26], which obtains burn width measurements by measuring DT γ's at DTn yields $> 10^{13}$. The comparison between GRH and PTOF is shown graphically in fig 9. GRH and PTOF generally agree within uncertainty, although there is discrepancy on shots N230708-001 and N230611-003. All shots are close to the yield floor of GRH so γ backgrounds can affect measurement– for instance, N230708-001 had a bright ARC source that may have interfered with GRH measurements of the DT γ's. On the PTOF side, it

TABLE III. PTOF-measured DTn burn widths and GRH-measured DTγ burn widths for a series of NIF shots. Ion temperature and yield data from NTOFs are also provided for each shot.

Experiment	W_{burn}^{PTOF} [ps]	W_{burn}^{GRH} [ps]	T_{DTn} [keV]	Y_{DTn}
N230313-002	1859	–	5.6	1.1e13
N230611-001	325	270	5.4	3.1e14
N230708-001	298	183	3.31	1.5e14
N230723-001	144	147	4.18	6.6e13
N231001-003	327	–	2.93	1.5e14
N240317-001	306	285	6.54	2.0e14

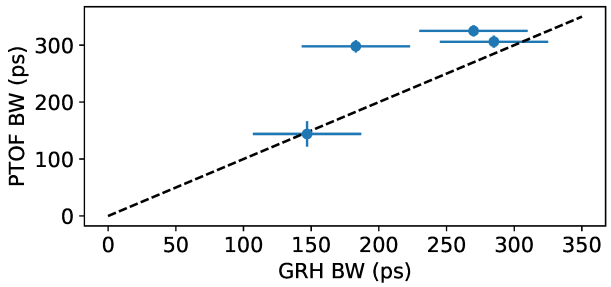

FIG. 9. GRH vs PTOF burn width values for shots on which both were measured

is possible there is excess broadening occurring not accounted for in table II, but this is in contrast with the fast rise observed for N230723-001 despite the same filter and detector setup. Work to reduce the width of the PTOF IRF through decreased detector capacitance and by eliminating potential sources of scatter like filtering will be done in the future to see if agreement with GRH is improved. Running PTOF on higher yield shots further from the GRH floor will also be attempted.

VI. PTOF IN CLOSE

Many of the error sources discussed in previous sections can be reduced with a smaller standoff distance of the detector – in particular, ion temperature uncertainty plays a smaller role with reduced standoff, as $\Delta W_{IRF,Ti}^2/W_{IRF}$ is proportional to the standoff distance. Additionally, W_{IRF} has a dependence on the time of flight broadening.

For DTn the standoff has only a modest effect on the error budget, since they move faster and incur less TOF broadening. However, for DDn at the typical 50 cm detector standoff distance, the time of flight broadening is increased to 500 ps and $\Delta W_{IRF,Ti}^2/W_{IRF}$ is increased to 13 ps. With these numbers the total squared error becomes $\sqrt{\Sigma \Delta W_{IRF}^2} \approx 130$ ps even without taking the increased scattering of neutrons in the filter into account. This makes measurement of short bang times very inaccurate.

Preliminary designs have been made for a bracket holding PTOF at 10 cm from target chamber center (TCC). At this standoff distance, DDn time of flight broadening is only 100 ps, similar to DTn at 50 cm standoff. Thus, bringing PTOF in close would allow for DDn burn widths to be measured at the NIF with similar accuracies to those provided in table II. Currently, no other diagnostic at the NIF is capable of making DDn burn width measurements. Additionally, the yield floor of PTOF would be lowered by a factor of 25, allowing bang time and burn width measurements on shots of much lower yield ($\sim 10^8$) than is currently possible for any diagnostic on the NIF.

Moving PTOF in closer does bring several challenges that must be addressed– in particular, debris flow can physically damage the detector, less time of flight separation between xray and neutron signals can complicate analysis if there is more overlap between the two signals, and the maximimum yield shots that can be measured while guaranteeing linear response falls from $\sim 10^{15}$ to $\sim 4 \times 10^{13}$ DT-n. The former two challenges are addressed by using a thick tungsten cap as blast shield/xray filter. Additionally, at very close standoff distances, clearance issues with other diagnostics become a concern which sets the lower bound close to 10 cm.

VII. PATH FORWARD

Aside from PTOF at 10 cm, several improvements to the PTOF system can be made that will enhance burn width measurement capability. The error budget in table II provides a suggestion as to what hardware and analysis upgrades would be most fruitful to pursue. First, improved knowledge of xray filter response using the methods from this paper would allow for reduced error since the filter response could be unfolded out of the measured timing shots. Secondly, enhanced understanding of diamond physics would help with selecting more high performing diamonds and reducing shot-to-shot variability seen in the rising edge of xray timing shots. Finally, reducing cable chain broadening would allow significantly faster signals to be analyzed with very small error, especially when coupled with PTOF in close. Without cable chain and TOF broadening, the rise time could approach the much faster 30 ps figures seen at MegaRay. One potential solution is to use electro-optical systems that convert the electrical signal to and from optical one that can be transported without dispersion. This technique has been successfully used for GRH on high yield shots, demonstrating reliability and robustness up to yields of 10^{15} DT-n[27]. With no cable chain response, the system resolution would be governed by the rise time of the detector by itself, which is < 50 ps for the PCDs considered in this paper, leading to $W_{IRF} \approx 2.091 \times 50ps \approx 100ps$, allowing for much more resolution for narrow burn width experiments.

In addition to shots on the NIF, another option with

a chance for higher data throughput would be fielding fast single crystal PTOF detectors at the OMEGA laser facility to benchmark burn width measurements as more campaigns are in a yield range favorable to simultaneous measurement of burn widths by PTOF and other diagnostics like the neutron temporal diagnostic[28].

VIII. CONCLUSION

PTOF is a diagnostic traditionally utilized for measuring nuclear bang times on low yield shots at the NIF. Recently, characterization of detectors at a high rep rate electron accelerator revealed detectors with an ultra-fast response and allowed in depth analysis of the behavior and contributing components of this response, allowing PTOF to measure the burn width of implosions with < 500 ps burn widths for the first time. These detectors have been extensively characterized suggesting that the fast response is the result of high concentrations of nitrogen acting as recombination sites and a fermi level close to the nitrogen trap level that facilitates recombination by both electrons and holes.

Several NIF shots have had burn widths measured using ultra-fast detectors and the PTOF values generally compare well with values measured from GRH for burn widths as low as 150 ps. A concept for fielding PTOF substantially closer to the implosion has also been presented, which would uniquely allow nuclear burn width measurements of DD-n.

IX. DATA AVAILABILITY

The data that support the findings of this study are available from the corresponding author upon reasonable request.

X. ACKNOWLEDGEMENTS

This work was performed under the auspices of the U.S. Department of Energy by Lawrence Livermore National Laboratory under Contract DE-AC52-07NA27344 and supported by LLNL contract B656484. B. Reichelt is supported by the DOE SSGF fellowship under contract DE-NA0003960. This report was prepared as an account of work sponsored by an agency of the United States Government. Neither the United States Government nor any agency thereof, nor any of their employees, makes any warranty, express or implied, or assumes any legal liability or responsibility for the accuracy, completeness, or usefulness of any information, apparatus, product, or process disclosed, or represents that its use would not infringe privately owned rights. Reference herein to any specific commercial product, process, or service by trade name, trademark, manufacturer, or otherwise does not necessarily constitute or imply its endorsement, recommendation, or favoring by the United States Government or any agency thereof. The views and opinions of authors expressed herein do not necessarily state or reflect those of the United States Government or any agency thereof. Approved for unlimited release – LLNL-JRNL-864526.

[1] H. Rinderknecht *et al.*, Review of Scientific Instruments **83** (2012).
[2] M. Pillon, M. Angelone, and A. Krasilnikov, "14 mev neutron spectra measurements with 4% energy resolution using a type iia diamond detector," Nuclear Instruments and Methods in Physics Research Section B: Beam Interactions with Materials and Atoms **101**, 473–483 (1995).
[3] G. Schmid, R. Griffith, N. Izumi, J. Koch, R. Lerche, M. Moran, T. Phillips, R. Turner, V. Y. Glebov, T. Sangster, *et al.*, "Cvd diamond as a high bandwidth neutron detector for inertial confinement fusion diagnostics," Review of scientific instruments **74**, 1828–1831 (2003).
[4] S. Agostinelli *et al.*, Nuclear instruments and methods in physics research section A: Accelerators, Spectrometers, Detectors and Associated Equipment **506**, 250–303 (2003).
[5] J. Allison *et al.*, IEEE Transactions on nuclear science **53**, 270–278 (2006).
[6] J. Allison *et al.*, Nuclear instruments and methods in physics research section A: Accelerators, Spectrometers, Detectors and Associated Equipment **835**, 186–225 (2016).
[7] M. Bethesda, ICRU report **50** (1999).
[8] S. M. Seltzer, Radiation research **136**, 147–170 (1993).
[9] Diamond and Related Materials **5**, 1450–1456 (1996).
[10] Y. Lawrence, B. Reichelt, C. Wink, G. Rigon, J. Ball, M. G. Johnson, C. Li, and J. Frenje, "Determination of the response for the national ignition facility particle time of flight (ptof) detector using single particle counting," Review of Scientific Instruments (submitted).
[11] T. Behnke, P. Hüntemeyer, A. Oh, J. Steuerer, A. Wagner, and W. Zeuner, Nuclear Instruments and Methods in Physics Research Section A: Accelerators, Spectrometers, Detectors and Associated Equipment **414**, 340–356 (1998).
[12] C. Canali, E. Gatti, S. F. Kozlov, P. F. Manfredi, C. Manfredotti, F. Nava, and A. Quirini, Nuclear Instruments and Methods **160**, 73–77 (1979).
[13] L. S. Pan, D. R. Kania, P. Pianetta, I. Ager, J. W., M. I. Landstrass, and S. Han, Journal of Applied Physics **73**, 2888–2894 (1993).
[14] Y. Zheng, C. Li, J. Liu, J. Wei, and H. Ye, Functional Diamond **1**, 63–82 (2022).
[15] W. Shockley and W. Read Jr, Physical Review **87**, 835 (1952).
[16] D. Kania, Laser and Particle Beams **9**, 91–97 (1991).
[17] B. Lombos, Canadian journal of chemistry **63**, 1666–1671 (1985).
[18] V. M. Le Corre *et al.*, ACS Energy Letters **6**, 1087–1094 (2021).
[19] N. Nahman, IRE Transactions on Circuit Theory **9**, 144–152 (1962).
[20] M. Stråål, I. Chmutin, A. Boldizar, *et al.*, Transactons of the Nordic Rheology Society **18**, 107–116 (2010).
[21] C. A. Balanis, (National Aeronautics and Space Administration, 1969).
[22] S. Kerr *et al.*, Physics of Plasmas **30** (2023).
[23] J. A. Kulesza *et al.*, Tech. Rep. LA-UR-22-30006, Rev. 1 (Los Alamos National Laboratory, Los Alamos, NM, USA, 2022).
[24] P. Virtanen *et al.*, Nature Methods **17**, 261–272 (2020).
[25] A. Moore *et al.*, Review of Scientific Instruments **92** (2021).
[26] H. W. Herrmann *et al.*, Journal of Physics: Conference Series **244**, 032047 (2010).
[27] Miller *et al.*, "Mach-zehnder recording systems for pulsed power diagnostics," Review of Scientific Instruments **83** (2012).
[28] C. Stoeckl *et al.*, Review of Scientific Instruments **87** (2016).